AIP | Review of Scientific Instruments

High-field magneto-thermo-mechanical testing system for characterizing multiferroic bulk alloys

Nickolaus M. Bruno, Ibrahim Karaman, Joseph H. Ross Jr., and Yuriy I. Chumlyakov

Citation: Review of Scientific Instruments **86**, 113902 (2015); doi: 10.1063/1.4934571
View online: http://dx.doi.org/10.1063/1.4934571
View Table of Contents: http://scitation.aip.org/content/aip/journal/rsi/86/11?ver=pdfcov
Published by the AIP Publishing

High-field magneto-thermo-mechanical testing system for characterizing multiferroic bulk alloys

Nickolaus M. Bruno,[1] Ibrahim Karaman,[1,2,a)] Joseph H. Ross, Jr.,[2,3] and Yuriy I. Chumlyakov[4]

[1]*Department of Mechanical Engineering, Texas A&M University, College Station, Texas 77843, USA*
[2]*Department of Materials Science and Engineering, Texas A&M University, College Station, Texas 77843, USA*
[3]*Department of Physics and Astronomy, Texas A&M University, College Station, Texas 77843, USA*
[4]*Siberian Physical Technical Institute, Tomsk State University, Tomsk 634050, Russia*

(Received 4 July 2015; accepted 13 October 2015; published online 11 November 2015)

Multiferroic *meta*-magnetic shape memory alloys are well known for exhibiting large magnetic field induced actuation strains, giant magnetocaloric effects, magneto-resistance, and structural and magnetic glassy behaviors. Thus, they are candidates for improving modern day sensing, actuation, magneto-resistance, and solid-state refrigeration processes. Until now, however, experimental apparatuses have typically been able to probe a limited ferroic parameter space in these materials, i.e., only concurrent thermal and mechanical responses, or magnetic and thermal responses. To overcome this barrier and better understand the coupling of multiple fields on materials behavior, a magneto-thermo-mechanical characterization device has been designed and implemented. This device is capable of compressing a specimen at load levels up to 5300 N collinearly with applied fields up to 9 T between temperatures of −100 °C and 120 °C. Uniaxial stress, strain, temperature, magnetic field, and the volumetric average magnetization have been simultaneously measured under mixed loading conditions on a NiCoMnIn *meta*-magnetic shape memory alloy and a few selected results are presented here. © *2015 AIP Publishing LLC.* [http://dx.doi.org/10.1063/1.4934571]

I. INTRODUCTION

Modern day materials science and engineering is faced with increasingly complex requirements for the characterization of advanced active materials. One particular group of active materials, namely, *meta*-magnetic shape memory alloys (MMSMAs), exhibit numerous scientifically interesting phenomena[1–5] including giant inverse magnetocaloric effect, magnetoresistance, and magnetically driven actuation that can be studied by measuring the thermal, mechanical, and magnetic loading histories across their ferroic phase transitions.[3] Elaborate experimental methods are needed to analyze coupled multi-field effects and, therefore, such studies are rarely reported in the literature.[6–9] Multi-field property measurements are increasingly sought after to understand the coupled material behaviors[3] and to calibrate constitutive models,[10–14] and thereby improve the active material response.

NiMnX alloy systems, where X is In, Sn, Sb, and Al are the most widely recognized MMSMAs.[15–18] MMSMAs undergo simultaneous thermoelastic (martensitic) and magnetic phase transitions. The martensitic phase transformation in MMSMAs is the result of a reversible change in crystal structure and is accompanied by a large recoverable shape change. At relatively high temperatures, MMSMAs are in the austenite (A) phase. Upon lowering the temperature, the martensite (M) phase forms resulting in what is known as the forward (A–M) martensitic transformation.[19] On heating back the alloy from martensite, the A phase is recovered by the reverse transformation (M–A).

Interestingly, in MMSMAs the M and A phases exhibit different magnetic ordering. In NiMnX (X = Sn, In, Sb) MMSMAs, for example, the austenite phase is usually ferromagnetic[16] and the martensite phase is a mixture of magnetic states that results in a non-magnetic bulk phase.[20] On the other hand, in compounds such as FeMnGa,[21] CoMnGe,[22] NiMnGa,[23] and $Gd_5(Si_{1-x}Ge_x)_4$,[24] the martensite phase is ferromagnetic and the austenite phase is only weakly magnetic. The complex nature of the thermal, magnetic, and mechanical couplings exhibited by these alloys lends the possibility for their implementation in numerous sensing, actuation, and refrigeration applications, and therefore, a test apparatus has been designed and implemented to better understand their unique functionalities. The magneto-thermo-mechanical characterization (MaTMeCh) device, introduced here, can operate under varying magnetic fields, stress, and temperature while simultaneously monitoring stress, strain, magnetization, and temperature; it can be utilized in characterizing actuation, sensing, mechanical energy harvesting, and ferrocaloric cooling capabilities of various materials.

II. *META*-MAGNETIC SHAPE MEMORY ALLOYS

A. The shape memory effect

The reversible and diffusionless thermoelastic martensitic phase transformations observed in MMSMAs can be induced by sweeping their temperature across a set of critical points. On cooling from the A phase, martensite

a)Author to whom correspondence should be addressed. Electronic mail: ikaraman@tamu.edu

begins to nucleate at the martensite start temperature, M_s, and finishes propagating through the microstructure at the martensite finish temperature, M_f. On heating, austenite starts to form at the austenite start temperature, A_s, and finishes its transformation at the austenite finish temperature, A_f. Identifying these transformation temperatures is often the aim of most MMSMA studies, and therefore, the MaTMeCh device introduced here lends the ability to heat and cool the MMSMA across its thermoelastic transition with and practically almost without externally applied stress. During load-biased thermoelastic transformations in MMSMAs, the high temperature austenite phase transforms to a martensite phase with specific crystallographic variants[3,25] and as a result, a transformation strain as large as 6.5% can be measured.[3] Similar transformation strains can also be achieved by heating (cooling) under magnetic fields. To measure these thermoelastic transformation strains (stresses), the MaTMeCh device was outfitted with displacement (load) sensors discussed in Sec. III C.

B. Superelasticity

Martensitic phase transitions in MMSMAs can also be triggered by applying a mechanical load to the austenite phase. The stress-induced martensite can be fully recovered upon the removal of the load, which is known as superelasticity. Mechanical load, magnetic field, and temperature strongly change the characteristics of the martensitic transformation, such as transformation temperatures, strains, and hysteresis,[3,7] and therefore, the MaTMeCh device was designed with the capability of performing isothermal compression or isofield stress tests with the loading capacity up to 5300 N.

C. Magnetic field induced transformations (MFITs) in *meta*-magnetic shape memory alloys

Martensitic transformation in MMSMAs can also be induced by applying a magnetic field at specific temperatures.[3] A completely reversible MFIT is possible, however, large magnetic fields are normally needed to achieve complete reversibility, i.e., complete recovery of the original phase on releasing the field. In NiMnX (X = Ga, In, Sn, Sb, Al) alloys, the MFIT is analogous to heating the martensite phase to austenite. Therefore, the MMSMA can exhibit large transformation strains across MFITs. The MaTMeCh device offers the ability to completely transform the MMSMA under magnetic fields as high as 9 T while simultaneously measuring the magnetization, uniaxial strain, and temperature under varying applied mechanical loads and magnetic fields.

III. THE MaTMeCh DEVICE

A. General description

The MaTMeCh device was designed and constructed to analyze and measure the multiferroic responses explained above. The completed test rig system, shown in Fig. 1, was capable of applying up to 330 MPa of uniaxial compressive stress to 4 mm × 4 mm × 8 mm samples, or maximum force of 5300 N, along its longitudinal direction. This maximal force corresponds to the design limit of the test rig. Magnetic field levels between 0 and 9 T were generated collinear to the mechanical load by an external superconducting magnet surrounding the mechanical load frame; this magnet solenoid is illustrated in Fig. 1. The magnet was a vertical field, Cryomagnetics Nuclear Magnetic Resonance (NMR) solenoid housed in a KD-601 Series liquid helium dewar on a 46 cm tall tripod along with a Cryomagnetics magnet controller power supply. Along the mechanical load train, the specimen temperature could be swept or set anywhere between −100 °C and 120 °C. Additionally, to prevent icing around the test rig's critical components and sensors, the sample chamber can be evacuated to a rough vacuum prior to experimentation by lowering the Lexan vacuum shield shown in Fig. 1. Additionally, an electric heater was added to the external housing (see Fig. 1) to protect the mechanical actuator and the NMR magnet dewar when testing at cryogenic temperatures.

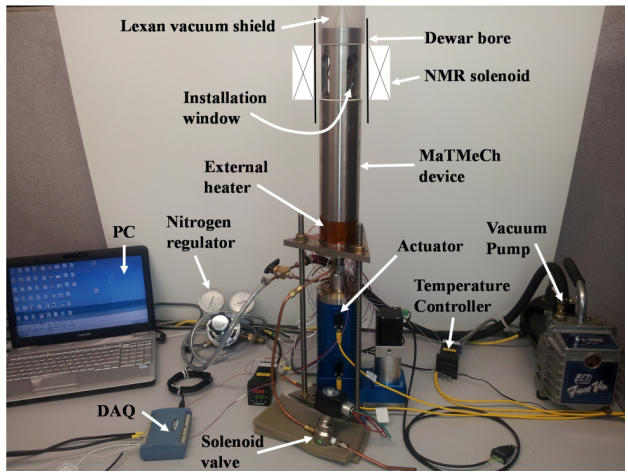

FIG. 1. The complete MaTMeCh device system showing the location of the superconducting solenoid during magnetic testing. Critical components are labeled and discussed in the text.

In Fig. 1, the PC, data acquisition hardware (DAQ), temperature controllers (PID), gas nitrogen regulator, actuator, vacuum pump, and cryogenic-rated solenoid valve for liquid nitrogen are all shown. These components remain outside the intense magnetic fields generated within the bore of the NMR magnet. The compression samples, discussed below, are installed into the test apparatus through the installation windows near the top of the MaTMeCh device depicted in Fig. 1. The samples were first installed before the rig was hoisted into the bore of the magnet.

Fig. 2(a) is a cross sectional illustration of the experimental apparatus in Fig. 1 and surrounding magnet liquid helium dewar. The MaTMeCh device housing, labeled as "1," was of grade 2 titanium construction for its strength, machinability, and non-magnetic behavior. Three windows were cut via electro-discharge machining (EDM) at the top of the housing intended for sample installation (Fig. 1) and the adjustment of sensors (not shown in Fig. 2(a)). Parts "2" and "3" are the bottom and top pushrods, respectively, machined from grade 2 Ti and copper-beryllium (Cu–Be) for thermal

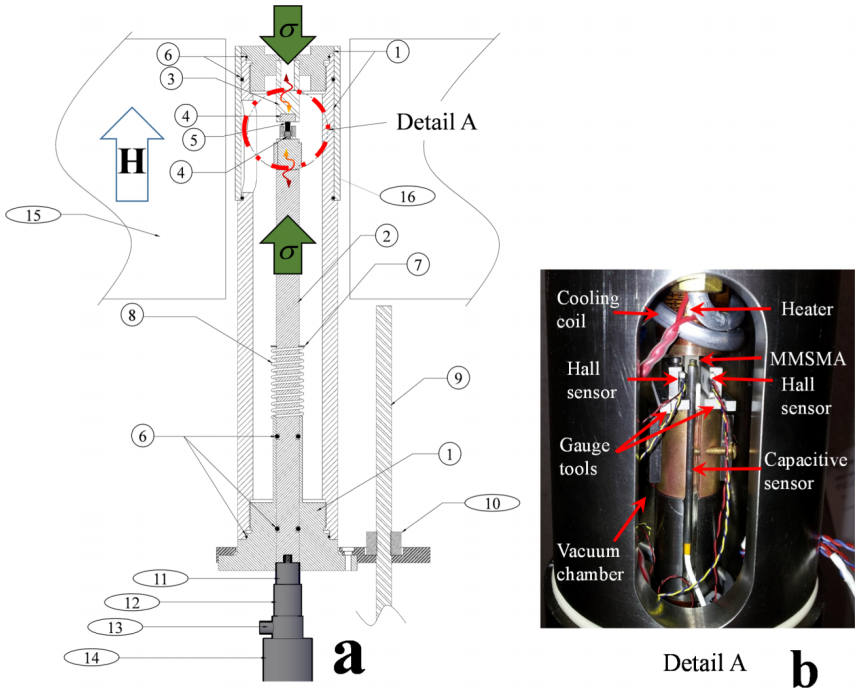

FIG. 2. A cross-sectional view of the magneto-thermo-mechanical characterization (MaTMeCh) device (a) in Fig. 1. Parts are labeled as 1: grade 2 titanium housing, 2: bottom push-rod, 3: upper push-rod, 4: ceramic inserts, 5: MMSMA specimen, 6: O-rings, 7: CuBe snap ring, 8: titanium spring, 9: acme threaded tension rod, 10: brass nut, 11: spherical Ti-6Al-4V connection piece, 12: flat Ti-6Al-4V connector, 13: load cell, 14: actuator thrust arm, 15: liquid helium dewar and NMR magnet solenoid, 16: Lexan vacuum cover. Detail A from (a) is depicted in (b) to clearly illustrate the specimen stage area during testing.

conductivity and strength. A Cu–Be snap ring and a custom titanium spring configuration (see parts 7 and 8 in Fig. 2(a)) were employed to apply a bias upward force of about 25 N on the MMSMA sample located in the section labeled "Detail A." This bias force was intended to keep the MMSMA stationary during complete mechanical unloading under high magnetic field levels. Ideally, the test frame was designed so that the compression sample would be positioned in the field center and no body forces would be generated due to field non-uniformity away from the field center. However, as a safety measure, the bias force was implemented. Additionally, the bias force lends the ability to load a new sample in the NMR magnet while a non-zero magnetic field is generated within the magnet bore.

Above and below the sample were high strength non-magnetic ceramic inserts (part 4 in Fig. 2(a)) which were employed due to the large local stress concentration generated by compressing a small rectangular sample. Non-magnetic metals would have plastically deformed if implemented, here, due to their relatively low yield strengths. Preliminary finite element simulations predicted approximately 1.4 GPa of local stress at the sample interface when 200 MPa was applied to the sample by the surrounding push rods. The bottom ceramic insert (custom sized Al_2O_3 bar) is visible in Fig. 2(b). Each component labeled in the schematic of Fig. 2(a) is described in the figure caption.

Individual components of the test frame were designed using AutoCAD 2014 and 3D models were converted to SolidWorks to be analyzed with the SolidWorks finite element analysis software. The Von-Mises stress of each load bearing piece was computed under the maximum design load of 5300 N and the computed Von-Mises stresses were compared with the yield strengths of the selected materials. A factor of safety of 1.5 was used in the design and sizing of the load bearing components.

A USB-2408 DAQ system with onboard cold-junction compensation was used to log the temperature, mechanical load, uniaxial displacement, stray magnetic field, and applied magnetic field with a custom designed LabVIEW program. The actuator supplying the mechanical compressive load communicates with the computer via a USB-RS485 converter and is controlled with the same custom LabVIEW program. Two programs were written; one was intended for superelastic loading up to a specified load limit and the other was used to hold the mechanical load constant during temperature sweeps or field ramping. The constant load LabVIEW sequence was programmed with displacement limits in the case of premature sample failure.

Sections III B–III D describe thermal, mechanical, and magnetic control and measurement systems in more detail. Additionally, the calibration for each loading type (i.e., temperature, mechanical load, and magnetic field) is briefly discussed and, finally, a few sample results of the MaTMeCh device are presented for a NiCoMnIn *meta*-magnetic shape memory alloy.

B. Thermal control and measurements

To measure the shape memory effect explained above, thermal sweeps of the compression samples were achieved via conduction through the compression rods. Non-magnetic polyimide ultra-thin heater sheets with adhesive backings were wrapped around the top (see Fig. 2(b)) and bottom compression rods. The top and bottom heaters were wired

in parallel such that activation/deactivation of the heaters occurred simultaneously via a CN8200 series OMEGA, Inc., PID controller. Heaters were wired using a 12-Cu lead vacuum feedthrough threaded into the bottom housing of the test rig (bottom of part 1 in Fig. 2(a)).

Conax Technologies non-magnetic 316SS vacuum feedthroughs were employed to make electric connections within the sample vacuum chamber. One feedthrough was used for wiring the heaters and other sensors, and the other housed six T-type thermocouple wire pairs. Thermocouple pairs were welded and then placed at various points in the sample chamber, as well as directly on the sample surface to monitor temperature.

Around the strip heaters, aluminum tubing was wound. Liquid nitrogen was flowed through a connection at the bottom of the sample chamber (bottom of part 1 in Fig. 2(a)), which in turn cooled the compression rods and conducted heat away from the sample. Rubber tubing was used for connections between aluminum windings. The surrounding environment was evacuated to rough vacuum during testing. After sample installation, the Lexan vacuum shield (part 16 in Fig. 2(a)) was lowered over the installation windows. An external cryogenic solenoid valve with 304SS non-magnetic construction was implemented to flow pressurized (0.4 MPa) liquid nitrogen through the aluminum tubing and was opened and closed via the same PID controller that activated the heaters. Nitrogen liquid/gas was channeled out the top of the test frame after cooling the internal parts (above Detail A in Fig. 2(a)). PID controllers were auto-tuned to identify integral and derivative parameters. A set-point was programmed into to the PID controllers for isothermal tests with the T-type thermocouple on the specimen supplying the temperature feedback. Additionally, a program was written in the PID controller between a lower and upper set-point such that the controller activated/deactivated the heaters and solenoid valve at appropriate times to achieve the temperature sweeps at a specified rate.

C. Mechanical load control and measurements

Uniaxial stress-strain was measured using an Interface WMC sealed stainless-steel mini load cell and a Capacitec HPC-40 series non-magnetic capacitive sensor, respectively. The load cell was limited to a maximum load of 8896 N and the capacitive sensor was capable of sensing distances up to 1.2 mm from the target ground plate. The load cell (part 13 in Fig. 2(a)) was located outside of the strong stray field generated by the NMR magnet (part 15 in Fig. 2(a)). The small stray field on the load cell generated by the magnet (~0.2 T), when ramped from 0 to 9 T, led to a small body force on the load cell determined by observations once the system was assembled. This produced errors in uniaxial stress measurements no larger than 5 MPa during field sweeping. Uniaxial displacement was measured with the capacitive sensor next to the sample as shown in Fig. 2(b). This configuration employed the top compression plate as the sensor electrical "ground" target plate. As such, any additional strain that developed along the load train was negated. It is important to note that capacitive sensors are immune to magnetic fields over a wide range of temperatures, but they are not immune to icing. At low temperatures, ice will form at the capacitive sensing tip and influence displacement readings. This problem was addressed by evacuating the sample chamber with a roughing pump prior to testing and flushing the chamber with dry nitrogen gas. The sample chamber was sealed after installation with the Lexan vacuum shield (see Fig. 1 and part 16 in Fig. 2(a)).

Finally, since MMSMAs can exhibit significant temperature changes (~8 K) from the stress-induced phase transformation and associated latent heat of transformation,[26] mechanical testing is often performed slowly, for isothermal tests, or quickly, for "adiabatic" tests.[26] Typically, mechanical tests involving shape memory alloys were considered isothermal when loaded at strain rates no faster than $5{\cdot}10^{-4}$ s^{-1}. In this study, specimens are strained no faster than $2.5{\cdot}10^{-4}$ s^{-1} to ensure the measured response was near isothermal.

A custom actuator was designed by Mechatronic Techniques, LLC under the given design constraints to supply a compressive force to the MMSMA. Once the MaTMeCh device was hoisted into the magnet bore, the actuator was slid into place (part 14 in Fig. 2(a)). The finished actuator is capable of applying a maximum of 5337 N of continuous force at every actuation velocity of interest and exhibits a 90 mm stroke to assist in positioning the MaTMeCh device to the appropriate height within the NMR magnet. A Nanotec PD4-N stepper motor drives a 1:100 gearbox reducer which then rotates the spindle drive via a belt. The gearbox slows the drive speed to rates acceptable for isothermal measurements as discussed later in the calibration section. As shown in Fig. 2(a), a spherical compression fitting (part 11) was designed and threaded to the load train such that the bottom pushrod only had one contact point with the mating actuator. This minimized torque on the load cell and ensured proper parallelism between the compression sample's edges and the compression plate. Additionally, the proper alignment prevented premature brittle fracture of the specimen.

D. Magnetic control and measurements

In conventional magnetometry, magnetization measurements rely on a changing magnetic flux. Either the magnetic field applied to the sample is pulsed, or the measured sample is vibrated, or extracted, through a set of inductive pickup coils. The voltage in the pickup coils is then used to measure magnetization. In the case of MMSMAs, however, the applied magnetic field is static and during the mechanical loading, here, the sample is unable to be vibrated or extracted from the magnetic field.

In a previous study,[27] it was shown that the volume average magnetization can be determined by measuring the DC stray magnetic field surrounding a rectangular sample. Soft magnetic materials (such as MMSMAs) demagnetize in the absence of a magnetic field. In the presence of a magnetic field, a demagnetizing field is generated surrounding the sample. A fully demagnetized rectangular sample is depicted in Fig. 3(a). Arrows within the magnetic domains represent local magnetization. The stray field surrounding the sample is at a minimum, and therefore, no magnetic flux lines are

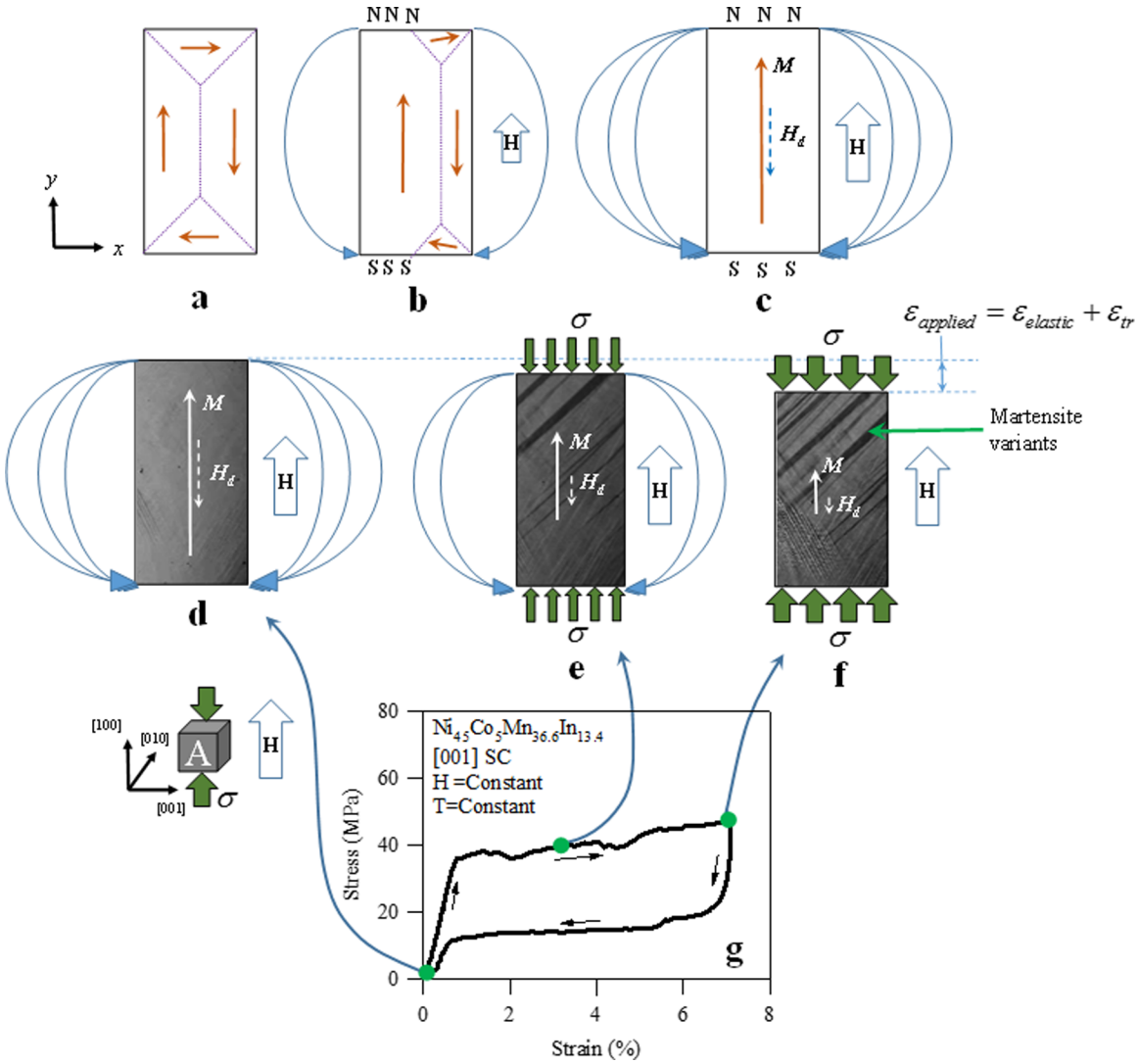

FIG. 3. A demagnetized (a), partially magnetized (b), and uniformly magnetized (c) bars in the y direction. Internal dashed lines indicate magnetic domain walls, blue external lines represent stray magnetic field, internal solid arrows indicate magnetic moments, and the dashed internal arrow indicates the internal demagnetizing field. The externally applied field is represented as H. A uniformly magnetized austenite MMSMA (d), mixed austenite and martensite (e), and fully martensite (f) magnetized bars depict superelasticity in constant magnetic field, H (g). Solid arrows at either edge of the rectangle represent compressive stress denoted as σ.

depicted. The MaTMeCh device is unable to measure a magnetic signal from the demagnetized sample depicted in Fig. 3(a).

A uniform magnetic field is longitudinally applied to the sample bar in Fig. 3(b). Upon applying the field, magnetic domains in the same direction of the applied field grow at the expense of the neighboring ones. The growth of the magnetic domain causes magnetic flux lines to appear surrounding the sample as a result of the north (N) and south (S) poles generated by the now averagely magnetized sample. This surrounding magnetic flux can be detected in the MaTMeCh device. The orientation of magnetic domains, stray field, and applied field in Fig. 3(c) matches those generated on the MMSMA sample during testing with the MaTMeCh device. This ideal geometry was used for computing the MMSMA magnetization from stray field measurements.

In the case where zero mechanical stress is applied to the MMSMA, it will magnetize in a uniform applied field as shown in Fig. 3(d) corresponding to the configuration in Fig. 3(c). Per the discussion above, the *meta*-magnetic transition in MMSMAs consists of concurrent magnetic and structural transitions. Figs. 3(d)-3(f) depict the evolution of the surrounding magnetic flux at different stages of the stress-induced *meta*-magnetic transition under a constant magnetic field, H. The magnetized austenite (Fig. 3(d)) begins to structurally transform to martensite upon mechanical loading. The temperature of the specimen in Figs. 3(d)-3(f) is such that superelasticity can be achieved. The magnetization of the sample is decreased as a result of the A–M transition, and is illustrated with fewer magnetic flux lines surrounding the specimen (Fig. 3(e)) as well as the martensite plates within the sample. Finally, when the stress-induced A–M transition is completed (Fig. 3(f)), the magnetic flux lines are virtually non-existent because the martensite phase in the illustrated MMSMA is non-magnetic.[20] Also note, the sample is uniaxially strained with increasing load. This is the strain generated across the superelastic loading, as shown in Figs. 3(f) and 3(g), and is the sum of elastic strain, $\varepsilon_{elastic}$, and

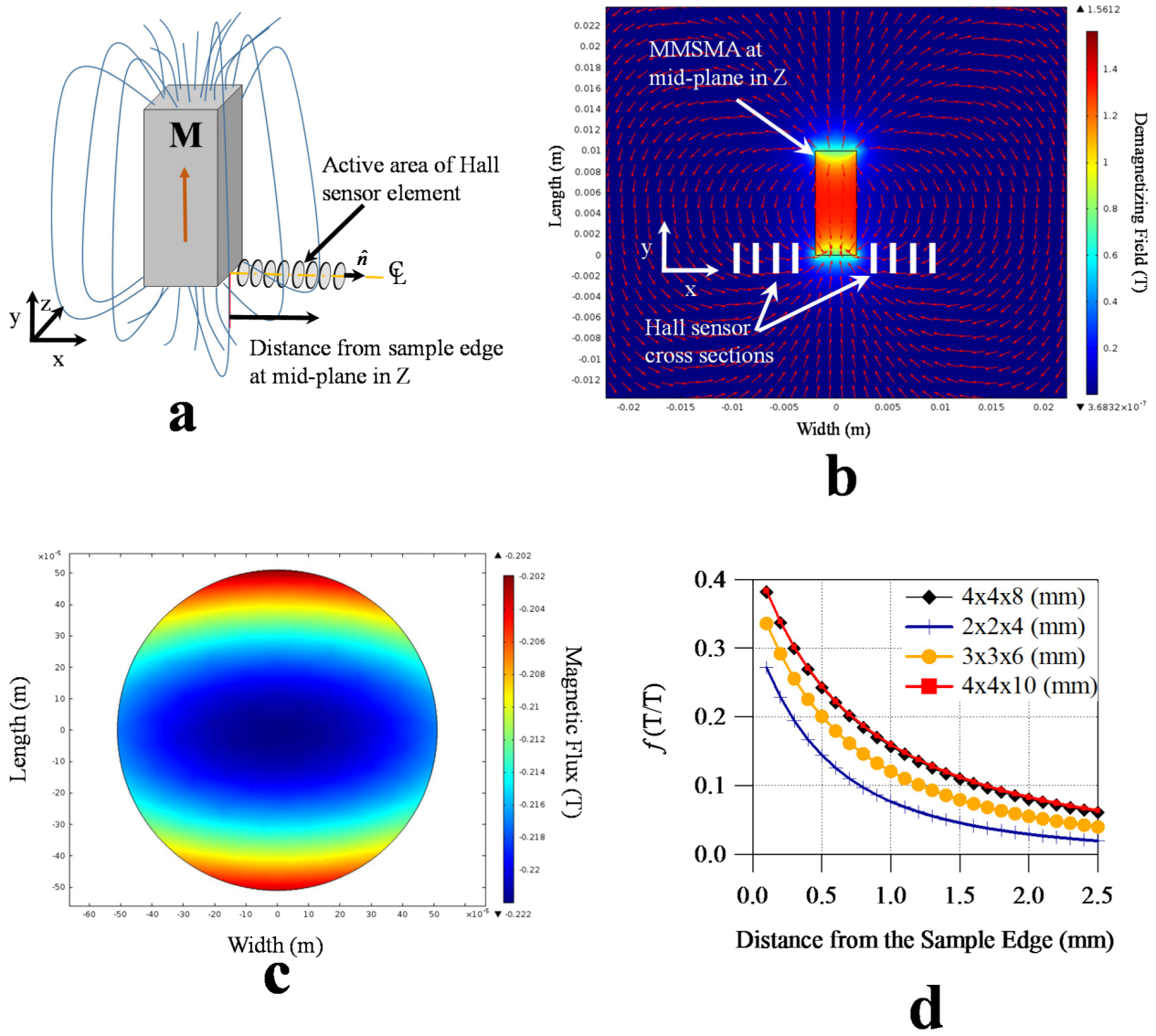

FIG. 4. The 3D simulation geometry (a) is illustrated for the fully magnetized MMSMA sample. Blue lines indicate magnetic flux and discs drawn with faces parallel to the sample surface represent the active Hall sensor element. The normal direction of the Hall elements is indicated along the centerline as $\hat{n}$. The bar is magnetized vertically in the finite element simulation. No external magnetic fields are applied. Magnetic field lines are represented as red arrows along a mid-plane slice of the sample in (b). White vertical lines near the south pole of the magnetized sample in (b) represent cross-sections of the discs illustrated in (a). The variation of the simulated magnetic field over the active Hall element in (a) is depicted in (c). The average magnetic field over the active Hall element was computed by integrating the field depicted in (c). The ratio of this x-direction integrated magnetic field over the disk areas in (c) with uniform vertical magnetization is plotted as a function of distance to the sample edge (see Eq. (1)) in (d). See text for details.

the martensitic transformation strain, ε_{tr}. These fundamental assumptions can be used to quantify the average sample magnetization of a uniformly magnetized MMSMA specimen during isothermal/isofield compression tests.

To measure the volume average magnetization of the MMSMA in the MaTMeCh device, during a compression test, the stray fields were measured with the use of cryogenic Hall sensors. A correlation between the horizontal field along the [001] direction (pictured in Fig. 3(d)) and a vertical magnetization in the [100] direction was predicted for an ideal case using finite element analysis. This correlation was then used for computing magnetization. Here, the magnetostatics module of COMSOL Multiphysics 4.3a software was employed for magnetic simulations.

The magnetic simulations consisted of a rectangular bar in free space that was uniformly magnetized along the longitudinal direction at 120 emu/g, i.e., 960 000 A/m, assuming a mass density of 8000 kg/m^3. These values are very close to those measured for the model MMSMA system used here, $Ni_{45}Co_5Mn_{36.6}In_{13.4}$.[3,7] The 3D simulation geometry is illustrated in Fig. 4(a). No magnetic fields were applied in the simulation, but rather a uniform magnetization in the sample geometry was applied in the "y" direction. Only the stray field resulting from the magnetization was computed in the simulations.

Circles representing the active area of the Hall element were drawn at various distances from the sample edge, such that the centerline of the circles corresponded to the mid-plane in the z direction, i.e., the middle of the bottom edge, of the magnetized bar. These are also illustrated in Fig. 4(a). Assuming the sample is uniformly magnetized in the y direction, a stray field is generated in the x direction as

shown by the red arrows in Fig. 4(b). Here, the demagnetizing field at the mid-plane (in z) is plotted and white vertical lines represent example locations of the simulated Hall sensor elements. As shown by the red arrows, some stray field passes perpendicularly through the Hall element. This magnetic field, B_X,was then integrated (see Fig. 4(c)) over the circular areas at various distances from the sample edge and the ratio between the measured field and the magnetization was computed as[27]

$$f = \frac{B_X}{\mu_0 M_y}. \quad (1)$$

In Eq. (1), B_X is the average magnetic field over the simulated circular area shown in Fig. 4(c), M_y was the average sample magnetization in A/m, and μ_0 is the permeability of free space. Interestingly, for a given distance from the sample surface, f remains nearly constant no matter what the magnetization level of the magnetized bar is (Fig. 4(d)). In other words, the horizontal field measured in the Hall elements varies linearly with sample magnetization at a constant location in space. The ratios computed with Eq. (1) are plotted in Fig. 4(d) as a function of distance from the sample edge for different specimen geometries. In practice, the M_y is unknown and B_X is measured at a set distance from the sample edge. The magnetization can then be computed using the simulated f values.

As shown in Fig. 4(d), the slope of f decays rapidly with increasing distance from the sample edge. This implies that minor errors in placement of the Hall sensors will result in large errors in the computed magnetization.[27] In this study, this error is minimized in three ways. First, an opposing Hall sensor configuration is employed as discussed in a previous work,[27] where it was shown that taking the average magnetization measurements from two Hall sensors equally spaced from the sample edge minimizes the error from misplacing a probe during experimentation. Second, the Hall elements were placed at 2.1 mm from the sample edge. As shown in Fig. 4(d), the slope of f is lower at further distances from the sample edge for a 4 mm × 4 mm × 8 mm test specimen. Finally, gauge tools, i.e., positioning forks, were cut from aluminum stock via wire EDM to ensure the Hall sensors were placed with an accuracy of 0.1 mm from the sample edge. These positioning forks are shown in Fig. 2(b).

Additionally, the thickness of the ceramic coating on the cryogenic Hall sensor was considered when designing the dimensions of the positioning forks. During compression, however, the MMSMA will strain laterally. The lateral strain was measured using a micrometer when the MMSMA was strained uniaxially up to 5% at room temperature and was determined to be only 0.25% (0.01 mm displacement), thus resulting in a negligible change in f during the compression tests in this study.

Here, two Lakeshore HGCT-3020 cryogenic Hall sensors were employed with a Lakeshore model 460 3-channel gaussmeter. The change of magnetic sensitivity of the sensors was approximately 0.1% across the temperature ranged considered here. The active area of the Hall sensors was reported to be 0.817 mm^2 by Lakeshore Cryotronics. An analog voltage was sent from the gaussmeter to the DAQ board which was then translated into stray field through a gaussmeter-defined calibration curve.

IV. CALIBRATION

A. Magnetic

To ensure that accurate magnetic measurements were collected with the MaTMeCh device, the field uniformity was first evaluated with the above mentioned Hall sensors. To measure the field, the sample was removed from the test rig and the Hall sensor was fixed (with Kapton tape) on the Al_2O_3 sample seat to measure the vertical field.

NMR magnets are capable of producing highly uniform fields, and in this case, the test rig was designed to be extended within the bore up to a limit, such that the compression sample was within the uniform field. Not only does this ensure the field generated by the magnet matches what is applied to the sample, but it also ensures that no body forces are generated by magnetic field gradients that could potentially move the sample during a test or generate internal stresses. In Fig. 5, the measured magnetic field within the bore of the magnet is plotted as a function of test frame extension. At 0, the test frame was fully extended. For all the tests performed, herein, the sample was located at −40 mm from full extension. This corresponded to approximately mid-stroke extension of the custom spindle drive actuator.

Next, the magnetization of whole compression specimens (~1 g in mass) was measured in a Quantum Design Magnetic Property Measurement System (MPMS3) vibrating SQUID magnetometer (SQUID-VSM). Measurements were collected at room temperature (~293 K) under 0.01 T. Longitudinally magnetizing the whole compression samples resulted in an averaged measured magnetic moment of 4.5 emu/g. This number served as a baseline for magnetic measurements. Before starting MaTMeCh tests, the field in the superconducting NMR magnet was set to 0.01 T and the LabVIEW-computed-magnetization was corrected by calibrating f such that the

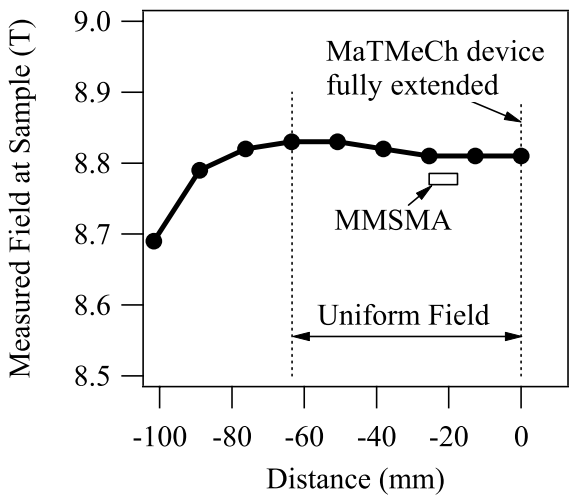

FIG. 5. Measured vertically applied magnetic field within the superconducting NMR magnet up to the full extension of the test frame. Field begins to significantly deviate at −63 mm from the full extension. All tests were performed at −40 mm of the full extension to ensure uniformity.

magnetization matched that reported by the SQUID-VSM under the same environmental conditions.

B. Mechanical

Calibration of the load cell was performed using a set of Instron calibration weights, however, the capacitive displacement sensor used for measuring uniaxial displacement was not re-calibrated from factory conditions. Since the linear actuator was a custom build from Mechatronic Techniques LLC, manual calibration was needed.

To determine a calibration curve for the spindle drive, a capacitive displacement sensor was attached to the drive head of the actuator and a conductive steel plate was mounted above the sensor to serve as the electrical ground target. The motor was then activated at different frequencies and the displacement of the drive head was recorded in time. The calibration curve of the linear actuator is shown in Fig. 6. As mentioned above, a typical strain rate employed for isothermal mechanical testing of MMSMAs is approximately $5{\cdot}10^{-4}$ s^{-1}. For an 8 mm long specimen, this nearly translates to 0.005 mm/s displacement rate. According to the calibration curve in Fig. 6, this corresponds to a motor rotation speed of 65 Hz. However, we chose to employ only 30 Hz in the compression experiments, described in Secs. V and VI, which corresponded to approximately 0.002 mm/s and thus the compression tests were kept isothermal.

V. MATERIALS PREPARATION

The $Ni_{45}Co_5Mn_{36.6}In_{13.4}$ alloy was fabricated via vacuum-induction melting. Single crystals were then grown from these melts with the Bridgman technique in a He environment. The composition of the single crystals was measured in a CAMECA SX-50 microprobe using wavelength dispersive spectroscopy (WDS) determined to be $Ni_{44.9\pm0.5}Co_{5.0\pm0.1}Mn_{36.0\pm0.4}In_{14.1\pm0.1}$ (at. %). Single crystal compression samples with the dimensions of 4 mm × 4 mm × 8 mm were cut using wire electro-discharge machining. The longitudinal direction of the compression samples was aligned with the [001] austenite crystal direction. This was to ensure that during magneto-thermo-mechanical testing, the magnetic field and mechanical load were applied in known crystal directions as represented in Figs. 3(d)-3(f). Each compression sample was homogenized at 900 °C for 24 h under partial argon atmosphere, water quenched, and then heat treated at 600 °C for 30 min to increase the austenite finish temperature by promoting a specific crystallographic ordering.[27]

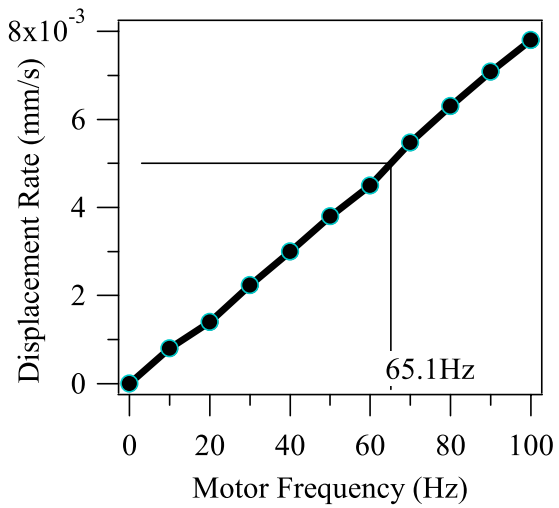

FIG. 6. The calibration curve for the custom spindle drive actuator designed specifically for the MaTMeCh device.

VI. EXPERIMENTAL RESULTS

A. Shape memory effect during load biased heating/cooling under magnetic field

Fig. 7(a) shows the measured shape memory effect of a $Ni_{45}Co_5Mn_{36.6}In_{13.4}$ (at. %) single crystal under 25 MPa compressive stress and 1 T applied field along the [001] austenite direction. The A_f temperature of this sample was tuned by annealing[28,29] to be 18 °C under zero stress and field condition. The sample is heated and cooled at 2 °C/min and was initially heated to 30 °C. At 30 °C, the sample exhibited a compressive strain equal to that generated by the elastic response of the austenite phase under 25 MPa and a magnetization level of approximately 91 emu/g. This magnetization level is comparable to SQUID measurements of austenite in samples with similar heat treatment and composition.[3,7,30] Upon cooling, the MMSMA transforms to its martensitic phase below 10 °C and exhibits approximately 5.7% transformation strain under the 25 MPa. The change in magnetization of 92 emu/g compares well with SQUID measurements performed under zero mechanical load. The small increase in magnetization from 30 °C to 10 °C, on cooling, can be attributed to cooling below the Curie point of austenite and promoting the magnetic order. As expected, the magnetic response of martensite is small, below 20 emu/g. Finally, it can be seen that the thermal hysteresis across the transformation is approximately 11 °C.

Across the temperature induced phase transformation, in Fig. 7(a), the load was held constant. The constant load is plotted as a function of temperature in Fig. 7(b). During heating and cooling, the MMSMA exhibited thermal expansion, and therefore, the spindle drive actuator constantly made adjustments to the applied mechanical load to account for load changes through the thermal expansion of the MMSMA. Through trial and error, the spindle drive control parameters were optimized for a specific heating/cooling and field ramping rate. The custom LabVIEW script sent the optimized control parameters to the spindle drive to adjust the stress under any given temperature and field ramping rate. As shown in Fig. 7(b), during most of the heating/cooling performed in Fig. 7(a), the stress was held constant within ±2.7 MPa of the given set-point. During the martensitic transformation, however, the stress deviated by as much as 4 MPa (see M–A in Fig. 7(b)) due to the rapid nucleation and propagation of the reverse (M–A) transformation. Nevertheless, the precision achieved with the custom linear actuator and LabVIEW script rivals the

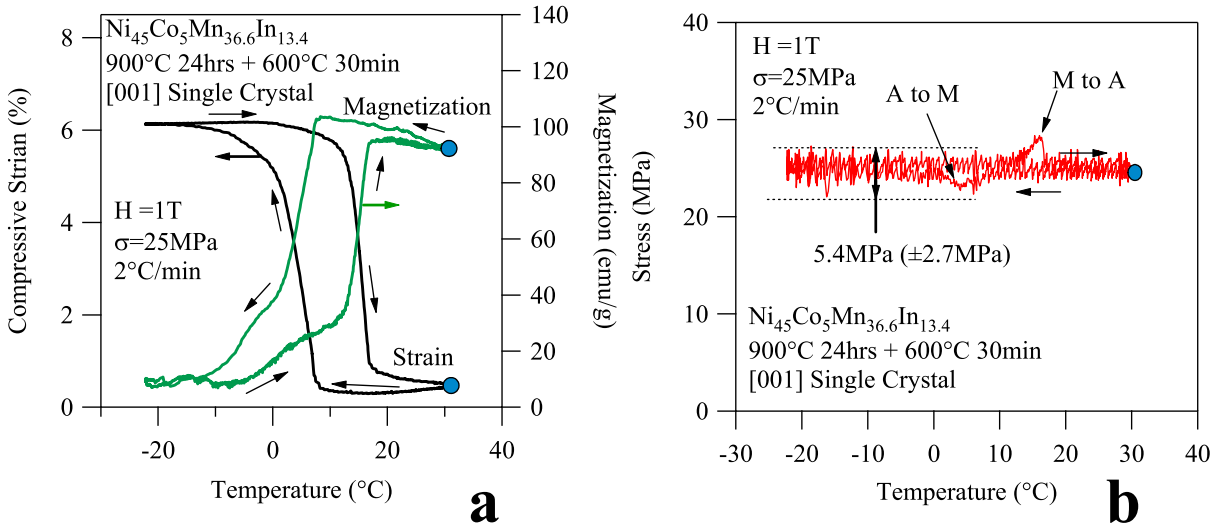

FIG. 7. The simultaneously measured uniaxial compressive strain and magnetization during heating and cooling at 2 °C/min through the martensitic transformation in a $Ni_{45}Co_5Mn_{36.6}In_{13.4}$ single crystal (a) and the corresponding constant-stress during the testing. During heating and cooling, the compressive load was held constant at 25 MPa with the custom LabVIEW script and the magnetic field was 1 T collinear to the [001] austenite crystal direction.

capabilities of other instrumentation that has been shown to hold a constant load during cryogenic thermomagnetic SQUID measurements.[7] Further testing similar to the one shown in Figs. 7(a) and 7(b) can allow the shape memory effect (SME) to be investigated under different fields and mechanical loads at different temperatures with high precision to study their influence on materials properties.

B. Superelasticity under magnetic field

Fig. 8(a) shows the measured superelastic responses of the $Ni_{45}Co_5Mn_{36.6}In_{13.4}$ single crystal at 18 °C under 0, 5, and 9 T applied field along the [100] austenite direction. In this particular material system, the A_f temperature in zero stress, or field, has been identified as 18 °C using SQUID-VSM. Upon compressing the sample, at critical stress levels of 40 MPa, 87 MPa, and 138 MPa, martensite begins to nucleate in the microstructure under 0, 5, and 9 T fields, respectively. Under normal conditions, the MMSMA can be loaded beyond the transformation strain limit to observe the elastic response of the stress-induced martensite. In this study, however, the material was not strained beyond 7% to protect its structural integrity. Loading the MMSMA further may produce premature brittle failure as documented in previous studies.[31]

As expected, when large magnetic fields are applied to the specimen, larger mechanical loads are needed to induce martensitic transformation.[3,7] The additional stress required to induce martensite for a given magnetic field, as compared to the field free condition, is known as magnetostress.[3,32] Future studies can be performed with the MaTMeCh device to fully explore the magnetostress trends in NiCoMnIn alloys

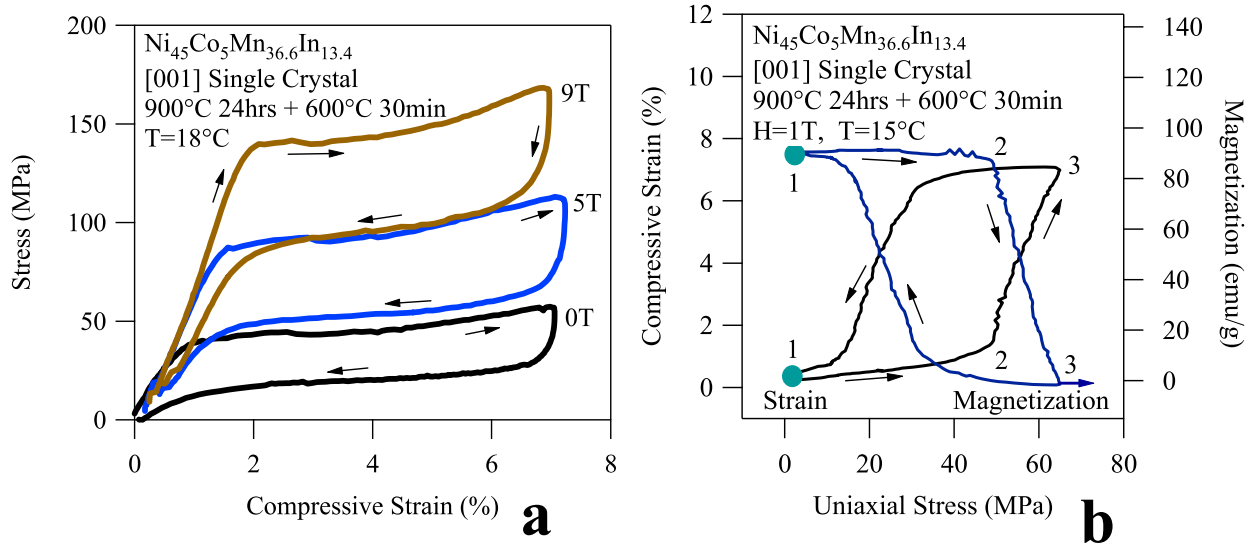

FIG. 8. The superelastic responses for $Ni_{45}Co_5Mn_{36.6}In_{13.4}$ single crystals compressed along the [001] austenite crystal direction under 0, 5, and 9 T fields; the test was conducted at 18 °C (a). The superelastic response and simultaneously measured stress-induced magnetization behavior are plotted in (b) for the same single crystal under 1 T at 15 °C.

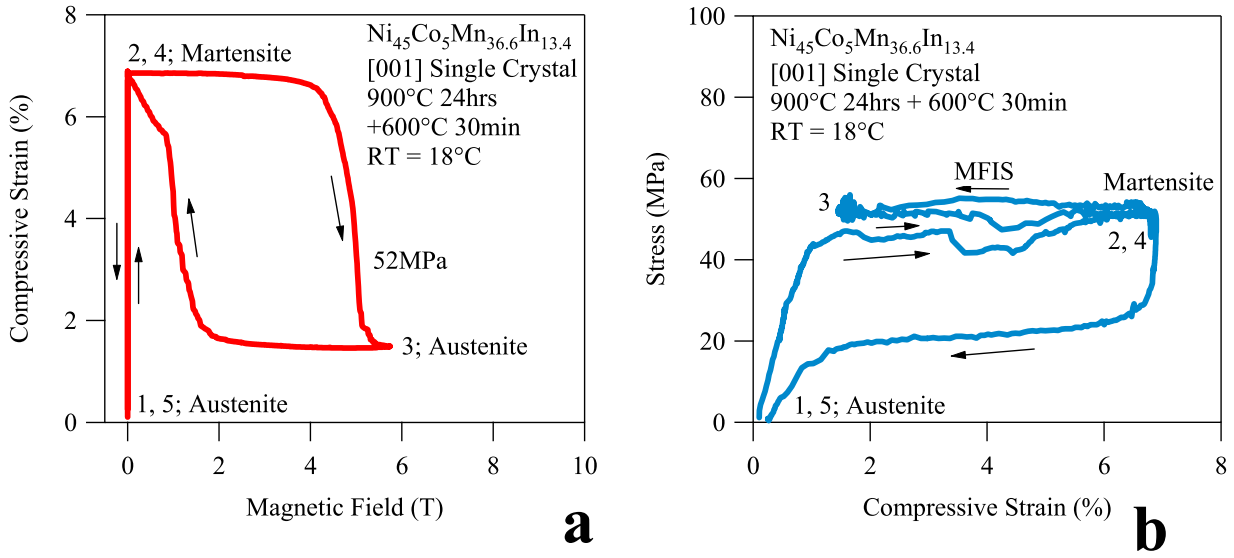

FIG. 9. The fully recoverable magnetic field induced strain (MFIS) in a $Ni_{45}Co_5Mn_{36.6}In_{13.4}$ single crystal uniaxially compressed under 52 MPa along the [001] austenite crystal direction (a) and the corresponding stress-strain data for the same test (b). The test was performed at 18 °C.

and other MMSMAs under various loading conditions and microstructures.

Finally, to demonstrate the magnetization measurement capabilities of the MaTMeCh device during isothermal/isofield compression, Fig. 8(b) shows the magneto-structural coupling of the same compression sample at 15 °C under 1 T applied field collinear to the load. The physical mechanisms describing this type of test are illustrated in Figs. 3(d)-3(f). Again, the sample was only compressed to 7% strain to prevent premature failure. Since 1 T was applied, the transformation temperatures of the MMSMA experienced a decrease, thus, the sample transforms from A to M at 50 MPa at 15 °C rather than 40 MPa (under 0 T) at 18 °C as illustrated in Fig. 8(a). From point 1 to 2 in the figure, the magnetic and linear elastic responses of austenite were measured. At a critical stress level (see points 2), the martensite nucleates and the magnetization level begins to decrease. After achieving nearly complete stress-induced martensite (around 7% total strain), the load is removed from point 3 to 1, and the magnetic response and sample geometry are fully recovered through superelasticity. The magnetization is measured to drop approximately 90 emu/g across the stress-induced martensitic transformation.

C. Magnetic field induced strain (MFIS)

The completely reversible magnetic field induced transformation under 52 MPa is shown in Fig. 9(a). Prior to field ramping, at 18 °C, the MMSMA was compressed to its martensitic state from austenite as shown by Fig. 9(b) (point 1 to 2). These points are also denoted in Fig. 9(a). Once the sample was almost completely comprised of stress-induced martensite (at point 2), the field was ramped from zero to 6 T (points 2 to 3) at approximately 50 Oe/s (0.3 T/min). This is comparable to the field ramping rates used in the above mentioned SQUID magnetometer for isothermal measurements. Under about 4.1 T, the field-induced M–A transition began and it finished around 5.3 T. On removing the field (point 3 to 4), the A–M transition began slightly below 2 T and completed around 0 T. The magnetic hysteresis under 52 MPa was measured to be nearly 4 T and the reversible MFIS was measured to be 5.4%. After reaching 0 T, the sample was comprised of stress-induced martensite again and the mechanical load was then removed (point 4 to 5). This recovered the austenite phase. The small deviations in stress from points 2 to 3 to 4 in Fig. 9(b) were caused by the rapid martensitic transformation. Further optimization of the linear actuator control parameters is needed to reduce these deviations in the load and future studies can be performed using the MaTMeCh device on MFITs under various mechanical loading conditions.

VII. SUMMARY AND CONCLUSIONS

A MaTMeCh device was designed, assembled, and implemented for studying the martensitic transformation behaviors of MMSMAs. The robust device accommodates −100 °C to 120 °C test temperatures, 0–5300 N uniaxial mechanical loads, and 0-9 T collinear-to-load magnetic fields. Uniaxial stress, strain, volume average magnetization, applied magnetic field, and temperature are measured simultaneously. The mechanical load, temperature, and magnetic field are driven independently, therefore, the MaTMeCh device is suitable for studying the effects of mixed loading conditions on single crystalline, or polycrystalline, compression bar samples. In this review, we discussed the shape memory effect, superelasticity, and magnetic field-induced *meta*-magnetic transitions and these served as a baseline for the MaTMeCh device design criteria. Finally, the testing capabilities were demonstrated by a few example data on an example MMSMA system, i.e., $Ni_{45}Co_5Mn_{36.6}In_{13.4}$ single crystals. Systematic studies are underway on $Ni_{45}Co_5Mn_{36.6}In_{13.4}$ single crystals to reveal the influence of multi-field loading on the martensitic transformation characteristics of MMSMAs.

ACKNOWLEDGMENTS

This work was supported by the U.S. National Science Foundation, Division of Materials Research, Metals and Metallic Nanostructures Program, Grant Nos. 1508634 and 1108396, the latter of which was under the umbrella of the Materials World Network Initiative. In addition, partial support from the National Science Foundation, under Grant No. DMR 08-44082 is acknowledged, which funds research in the International Materials Institute for Multi-functional Materials for Energy Conversion (IIMEC) at Texas A&M University. J.H.R. also acknowledges partial support from the Robert A. Welch Foundation (Grant No. A-1526). N.M.B. would like to also acknowledge Brent McMillan and Mechatronic Techniques for developing the custom spindle drive actuator used with the MaTMeCh device, Robert Barber for fruitful design discussions and SolidWorks FEA modeling, and Professor Tom Shield for personal communications regarding magnetic measurements.

[1]R. Kainuma, Y. Imano, W. Ito, H. Morito, Y. Sutou, K. Oikawa, A. Fujita, K. Ishida, S. Okamoto, and O. Kitakami, Appl. Phys. Lett. **88**, 192513 (2006).
[2]N. M. Bruno, C. Yegin, I. Karaman, J. H. Chen, J. H. Ross, J. Liu, and J. G. Li, Acta Mater. **74**, 66 (2014).
[3]H. E. Karaca, I. Karaman, B. Basaran, Y. Ren, Y. I. Chumlyakov, and H. J. Maier, Adv. Funct. Mater. **19**, 983 (2009).
[4]J. I. Perez-Landazabal, V. Recarte, V. Sanchez-Alarcos, S. Kustov, D. Salas, and E. Cesari, Intermetallics **28**, 144 (2012).
[5]X. B. Ren, Phys. Status Solidi B **251**, 1982 (2014).
[6]H. E. Karaca, I. Karaman, B. Basaran, Y. J. Chumlyakov, and H. J. Maier, Acta Mater. **54**, 233 (2006).
[7]J. A. Monroe, I. Karaman, B. Basaran, W. Ito, R. Y. Umetsu, R. Kainuma, K. Koyama, and Y. I. Chumlyakov, Acta Mater. **60**, 6883 (2012).
[8]H. E. Karaca, I. Karaman, B. Basaran, D. C. Lagoudas, Y. I. Chumlyakov, and H. J. Maier, Acta Mater. **55**, 4253 (2007).
[9]P. Mullner, V. A. Chernenko, and G. Kostorz, J. Appl. Phys. **95**, 1531 (2004).
[10]K. Haldar, D. C. Lagoudas, and I. Karaman, J. Mech. Phys. Solids **69**, 33 (2014).
[11]K. Haldar and D. C. Lagoudas, Proc. R. Soc. A **470**, 2169 (2014).
[12]N. M. Bruno, C. Ciocanel, H. P. Feigenbaum, and A. Waldauer, Smart Mater. Struct. **21**, 094018 (2012).
[13]B. Kiefer and D. C. Lagoudas, Philos. Mag. **85**, 4289 (2005).
[14]B. Kiefer, H. E. Karaca, D. C. Lagoudas, and I. Karaman, J. Magn. Magn. Mater. **312**, 164 (2007).
[15]R. Kainuma, K. Ito, W. Ito, R. Y. Umetsu, T. Kanomata, and K. Ishida, Mater. Sci. Forum **635**, 23 (2009).
[16]R. Kainuma, Y. Imano, W. Ito, Y. Sutou, H. Morito, S. Okamoto, O. Kitakami, K. Oikawa, A. Fujita, T. Kanomata, and K. Ishida, Nature **439**, 957 (2006).
[17]Y. Sutou, Y. Imano, N. Koeda, T. Omori, R. Kainuma, K. Ishida, and K. Oikawa, Appl. Phys. Lett. **85**, 4358 (2004).
[18]R. Kainuma, H. Nakano, and K. Ishida, Metall. Mater. Trans. A **27**, 4153 (1996).
[19]K. Otsuka and C. M. Wayman, *Shape Memory Materials* (Cambridge University Press, Cambridge, New York, 1998).
[20]M. Acet and E. F. Wassermann, Adv. Eng. Mater. **14**, 523 (2012).
[21]W. Zhu, E. K. Liu, L. Feng, X. D. Tang, J. L. Chen, G. H. Wu, H. Y. Liu, F. B. Meng, and H. Z. Luo, Appl. Phys. Lett. **95**, 222512 (2009).
[22]J. Liu, K. Skokov, and O. Gutfleisch, Scr. Mater. **66**, 642 (2012).
[23]A. Sozinov, A. A. Likhachev, N. Lanska, and K. Ullakko, Appl. Phys. Lett. **80**, 1746 (2002).
[24]V. K. Pecharsky and K. A. Gschneidner, Phys. Rev. Lett. **78**, 4494 (1997).
[25]H. E. Karaca, I. Karaman, A. Brewer, B. Basaran, Y. I. Chumlyakov, and H. J. Maier, Scr. Mater. **58**, 815 (2008).
[26]E. Bonnot, R. Romero, L. Manosa, E. Vives, and A. Planes, Phys. Rev. Lett. **100**, 125901 (2008).
[27]T. W. Shield, Rev. Sci. Instrum. **74**, 4077 (2003).
[28]N. M. Bruno, Ph.D. dissertation, Texas A&M University, 2015.
[29]J. A. Monroe, J. E. Raymond, X. Xu, M. Nagasako, R. Kainuma, Y. I. Chumlyakov, R. Arroyave, and I. Karaman, "Multiple ferroic glasses via ordering," Acta Mater. **101**, 107 (2015).
[30]J. Liu, T. Gottschall, K. P. Skokov, J. D. Moore, and O. Gutfleisch, Nat. Mater. **11**, 620 (2012).
[31]Y. J. Huang, Q. D. Hu, N. M. Bruno, J.-H. Chen, I. Karaman, J. H. Ross, Jr., and J. G. Li, Scr. Mater. **105**, 42 (2015).
[32]J. A. Monroe, J. Cruz-Perez, C. Yegin, I. Karaman, A. B. Geltmacher, and R. Kainuma, Scr. Mater. **67**, 116 (2012).